



# Performance enhancement of trimetallic nanoparticles in photocatalysis through chemical etching

Yu-Chun Cheng · Yun-Qi Dou · Tian-Song Deng

Received: 13 January 2025 / Accepted: 9 June 2025  
© The Author(s), under exclusive licence to Springer Nature B.V. 2025

**Abstract** Trimetallic nanoparticles have shown significant potential as multifunctional nanomaterials due to their superior photocatalytic performance, making them highly promising in materials science and nanotechnology. In this study, we designed and synthesized a trimetallic nanostructure consisting of a gold nanorod (Au NR) core, a silver (Ag) intermediate shell, and a silver-platinum (AgPt) alloy outer layer. The Au@Ag core-shell structure was first prepared by depositing silver onto the Au NR surface through a reduction reaction. Subsequently, an AgPt alloy was deposited via a reduction and replacement process, followed by oxidative etching to remove excess silver, resulting in the etched trimetallic nanostructure (Au@AgPt-E). Using methylene blue (MB) as the model system, the photocatalytic activity of Au@AgPt-E under visible and near-infrared light irradiation was significantly enhanced, achieving a rate 4.19 times higher than Au@Ag@AgPt and 7.67 times higher than single-metal Au NRs. The performance enhancement is primarily attributed to the surface plasmon resonance (SPR) effect generated

by the gold nanorod core in Au@AgPt-E. The SPR effect significantly enhances the light absorption of the gold nanorods, especially within specific wavelength ranges, allowing for efficient conversion of light energy into heat. This energy conversion process not only improves thermal efficiency but also facilitates the generation and separation of charge carriers, thereby increasing the efficiency of the catalytic reaction. Additionally, the Au@AgPt-E undergoes an etching process, which increases the number of catalytic active sites on the AgPt shell, further enhancing the catalytic performance. The combined effects of these factors result in a significant improvement in the material's performance. This study provides a novel approach for developing efficient plasmon-mediated photocatalysts and demonstrates broad application prospects in photocatalytic reduction processes.

**Keywords** Trimetallic nanoparticles · Gold nanorods · Silver-platinum alloy · Surface plasmon resonance · Photocatalysis · Oxidative etching

**Supplementary Information** The online version contains supplementary material available at <https://doi.org/10.1007/s11051-025-06374-3>.

Y.-C. Cheng · Y.-Q. Dou · T.-S. Deng (✉)  
School of Electronics and Information Engineering,  
Hangzhou Dianzi University, Hangzhou, P.R. 310018,  
China  
e-mail: dengts@pku.edu.cn

## Introduction

The extinction spectrum of Au NRs exhibits two prominent surface plasmon resonance peaks within the visible light range: transverse SPR and longitudinal SPR. The transverse SPR wavelength range is approximately 500–600 nm, while transverse SPR can be extended from 600 to 1200 nm by adjusting

the aspect ratio of Au NRs [1]. The tunable nature of SPR and its strong local electromagnetic field enhancement effect make it valuable for applications such as photocatalysis [2–5], surface-enhanced Raman scattering (SERS) [6–9], plasmon-enhanced fluorescence [10–13], photodetection, photothermal therapy [14–17], and biomedical applications [16, 18–20].

Bimetallic nanoparticles based on Au NRs have garnered significant attention due to their unique catalytic [21–24], optical [25–27], and electrical properties [28–31], which are strongly influenced by their morphology and structure. Among these properties, catalysis has been a key focus of research. Au NRs can be combined with one or more noble metals to form structures such as Au@Ag, Au@Pt, and Au@Pd, thereby integrating the properties of these materials. Platinum (Pt) has become a powerful electrocatalyst widely used in alcohol oxidation [32, 33] and hydrogenation reactions [34, 35] due to its unique physical and chemical properties. Studies have shown that combining Pt with Au NRs can significantly enhance the catalytic performance [36, 37].

Compared to bimetallic nanostructures, trimetallic nanoparticles based on Au NRs have garnered widespread attention in recent years due to their unique catalytic, optical, and electrical properties, which are largely influenced by their morphology and structure. Especially in terms of catalytic performance, Au NRs combined with other metals (such as silver, platinum, and palladium) can form composite trimetallic structures. These structures integrate the advantages of each component material, while the alloy structures are generally more stable in terms of chemical properties compared to monometallic ones. These combinations include single-phase alloy structures and core-shell structures, particularly those formed by using Au NRs as the core and coating an alloy shell on their surface to create a core-shell trimetallic structure. The Au@PdPt and Au@AgPt structures formed by combining Au NRs with PdPt and AgPt alloys have been widely applied in catalysis [38, 39] and sensors [40, 41] due to their excellent chemical stability and conductivity. These structures fully utilize the LSPR effect of Au NRs and the high conductivity and reactivity of the PdPt and AgPt alloy, effectively improving catalytic efficiency.

In our experiment, we successfully synthesized the target material Au@AgPt-E, utilizing the excellent

surface plasmon resonance effect of Au NRs and the hollow nanostructure of the AgPt shell, which provided more active sites. Additionally, through catalytic experiments with methylene blue (MB), we verified the material's superior photocatalytic performance, with an enhancement of up to 4.19 times compared to the unetched material. At the same time, we conducted finite-difference time-domain (FDTD) simulations of the material before and after etching, and the results showed that the etched material exhibited a higher electric field enhancement effect compared to the unetched material.

In the field of large-scale wastewater treatment, TiO<sub>2</sub> has been widely used due to its low cost and non-toxicity. However, its limitations, such as the ability to only absorb ultraviolet light, a high electron-hole recombination rate, and low catalytic efficiency, restrict its effectiveness in large-scale applications. On the other hand, the Au@AgPt-E catalyst, through the surface plasmon resonance effect, can enhance visible light absorption, expand the light response range, and has higher electronic conductivity, effectively reducing charge carrier recombination, thereby significantly improving photocatalytic efficiency. Its stronger catalytic performance and higher stability make it promising for large-scale wastewater treatment applications. Future research will focus on further optimizing its synthesis process and structural design, expanding its potential in a wider range of photocatalytic applications, and providing a promising approach for the design of efficient multifunctional nanocatalysts.

## Experimental section

### Materials

The chemicals used in this study were of high purity and required no additional purification. These included hexadecyltrimethylammonium bromide (CTAB, >98.0%), sodium oleate (NaOL, >97.0%), hydrogen tetrachloroaurate trihydrate (HAuCl<sub>4</sub>·3H<sub>2</sub>O), L-ascorbic acid (BioUltra, >99.5%), silver nitrate (AgNO<sub>3</sub>, >99%), sodium borohydride (NaBH<sub>4</sub>, 99%), iron nitrate nonahydrate (Fe(NO<sub>3</sub>)<sub>3</sub>·9H<sub>2</sub>O, 99%), nitric acid (HNO<sub>3</sub>, 67% in water), hydrochloric acid (HCl, 37 wt.% in water), hexadecyltrimethylammonium chloride (CTAC,

>99.0%), potassium tetrachloroplatinate ( $K_2PtCl_4$ , >99.99%), absolute methanol (MeOH), and methylene blue (MB). All the chemicals were purchased from Aldrich. Ultrapure water obtained from a Milli-Q Integral system was used in all experiments. The high purity of these chemicals ensured the reliability and reproducibility of the experimental results.

### Synthesis of Au NRs

The seed solution for the growth of Au NRs was prepared as follows: Initially, 0.25 mL of 10 mM  $H AuCl_4$  was mixed with 10 mL of a 0.1 M CTAB solution in a 20-mL scintillation vial. Subsequently, 0.6 mL of freshly prepared 0.01 M  $NaBH_4$  was diluted to 1 mL with water and injected into the Au (III)-CTAB solution with vigorous stirring at 1200 rpm. The solution changed in color from yellow to brownish yellow, and stirring was halted after 2 min. The seed solution was then allowed to age at room temperature for 30 min before further use. To prepare the growth solution, 7.0 g of CTAB (resulting in a final concentration of 0.037 M in the growth solution) and 1.234 g of NaOL were dissolved in 250 mL of warm water (approximately 50 °C) in a 1-L Erlenmeyer flask. The solution was allowed to cool down to 30 °C, and a 4 mM  $AgNO_3$  solution was introduced. The mixture was left undisturbed at 30 °C for 15 min, following which 250 mL of a 1 mM  $H AuCl_4$  solution was added. The solution became colorless after 60 min of stirring at 700 rpm. To adjust the pH, 2.1 mL of HCl (37% wt. in water, 12.1 M) was added. After an additional 15 min of slow stirring at 800 rpm, 1.25 mL of 0.064 M AA was introduced, and the solution was vigorously stirred for 30 s. Finally, a small amount of the seed solution was injected into the growth solution. The resulting mixture was stirred for 30 s and left undisturbed at 30 °C for 12 h to facilitate the growth of nanorods. The final products were isolated by centrifugation at 8000 rpm for 15 min, followed by removal of the supernatant. No size and/or shape-selective fractionation was performed in this process.

### Synthesis of Au@Ag nanostructures

The as-prepared Au NRs solution had a volume of approximately 500 mL. Subsequently, the Au NRs were subjected to purification twice by centrifugation at 7000 rpm for 30 min, followed by the removal

of the supernatant. The resulting solution, which was concentrated 10 times, was stored in a solution containing 30 mM CTAB as the stock solution. To deposit Ag onto the surface of the Au NRs, 0.1 mL of the Au NR stock solution was added to a mixture containing 3.4 mL of 30.0 mM CTAC. The combined solution was then heated in a 60 °C water bath for 20 min. Following this step, 0.05 mL of 100 mM AA and 0.16 mL of 8.0 mM  $AgNO_3$  were introduced into the solution, which was maintained in a 60 °C water bath for an additional 30 min. Subsequently, the Au@ $Ag_{360}$  nanostructures were obtained.

### Synthesis of Au@Pt nanostructures

The as-prepared Au NRs solution had a volume of approximately 500 mL. Subsequently, the Au NRs were subjected to purification twice by centrifugation at 7000 rpm for 30 min, followed by the removal of the supernatant. The resulting solution, which was concentrated 10 times, was stored in a solution containing 30 mM CTAB as the stock solution. To deposit Pt onto the surface of the Au NRs, 0.1 mL of the Au NR stock solution was added to a mixture containing 3.4 mL of 30.0 mM CTAC. The combined solution was then heated in a 60 °C water bath for 20 min. Following this step, 0.05 mL of 100 mM AA and 0.01 mL of 10.0 mM  $K_2PtCl_4$  were introduced into the solution, which was maintained in a 60 °C water bath for an additional 30 min. Subsequently, the Au@Pt<sub>25</sub> nanostructures were obtained.

### Synthesis of Au@Ag@AgPt nanostructures

To create varied morphologies of Au@Ag@AgPt nanostructures, 0.01 mL of a 10 mM  $K_2PtCl_4$  solution was introduced into the Au@Ag solution and incubated in a 60 °C water bath for 20 min. Subsequently, the solution was harvested following two rounds of centrifugation at 7000 rpm for 30 min. We adjust the amounts of  $AgNO_3$  (from 0.02 to 0.80 mL),  $K_2PtCl_4$  (from 0.01 to 0.40 mL), AA, and reaction temperature.

### Synthesis of Au@AgPt-E nanostructures

Begin by adding 0.1 mL of a 20 mM  $Fe(NO_3)_3$  solution and 0.2 mL of a 20 mM  $HNO_3$  solution to the Au@Ag@AgPt solution, followed by the addition of

10 mL of water. Subsequently, allow the mixture to stand under 600 rpm conditions for 4 h. Afterward, remove any excess reagents through centrifugation and store the Au@AgPt-E nanostructures in water.

### Photocatalysis

Briefly, 1 mL of 0.01 mM MB was mixed with 0.1 mL of 0.1 M freshly prepared NaBH<sub>4</sub>, then 10 μL different kinds of materials solutions were added to the mixed solution. We used the above catalytic experimental steps on the basis of the illumination with a 250-W Xenon lamp (HDL-II, Suzhou Betical Optoelectronics Technology Co. Ltd, China). We measured the extinction spectra of the solution at 2-min intervals until the peak corresponding to 628 nm disappeared. The MB concentration was determined at the wavelength of 628 nm using a UV-vis spectrophotometer (UV-1900i, Shimadzu). The reaction was maintained at normal atmospheric temperatures.

### Characterization

Optical extinction spectra were recorded with a UV-1900i spectrophotometer (Shimadzu, Japan) with a 10-mm optical path. The transmission electron microscopy (TEM) images were obtained with an HT-7700 microscope (Hitachi, Japan) operating at a voltage of 100 kV. Energy-dispersive spectroscopy (EDS) mapping was performed using a ZEISS SEM Sigma 300 (Germany). The particle sizes of the nanoparticles were measured from TEM images using ImageJ software, whereby > 100 nanoparticles were measured for each sample.

### FDTD simulations

Finite difference time domain (FDTD) is a method for solving Maxwell's equations on a discretized spatial grid in complex geometries. The FDTD simulations were carried out with commercial software (Lumerical FDTD Solutions). A total field scattered field source was used to simulate a propagating plane wave interacting with the nanostructures, with a wavelength range of 300 – 1100 nm. A three-dimensional nonuniform mesh was used, and a grid size of 0.6 nm was chosen for calculating the spectra and the electric field distribution of Au NRs, Au@Ag<sub>360</sub>, and Au@Ag<sub>360</sub>Pt<sub>25</sub>-E. In order to observe a more credible

spectra, we choose Au NR with similar aspect ratio in the simulations. The dielectric functions of Au NR and Pt were obtained by fitting the points from the data of Babar [42]. We use the effective medium approximation (EMA) based on the Maxwell–Garnett equation to calculate the effective dielectric function of the AgPt alloy [43]

$$\rho \frac{\epsilon_{eff} - \epsilon_{Ag}}{\epsilon_{eff} + 2\epsilon_{Ag}} + (1 - \rho) \frac{\epsilon_{Pt} - \epsilon_{Ag}}{\epsilon_{Pt} + 2\epsilon_{Ag}} = 0 \quad (1)$$

Thus, the effective dielectric functions of AgPt alloy are given by

$$\epsilon_{eff} = \epsilon_{Ag} \frac{2\rho(\epsilon_{Pt} - \epsilon_{Ag}) + \epsilon_{Pt} + 2\epsilon_{Ag}}{2\epsilon_{Ag} + \epsilon_{Pt} - \rho(\epsilon_{Pt} - \epsilon_{Ag})} \quad (2)$$

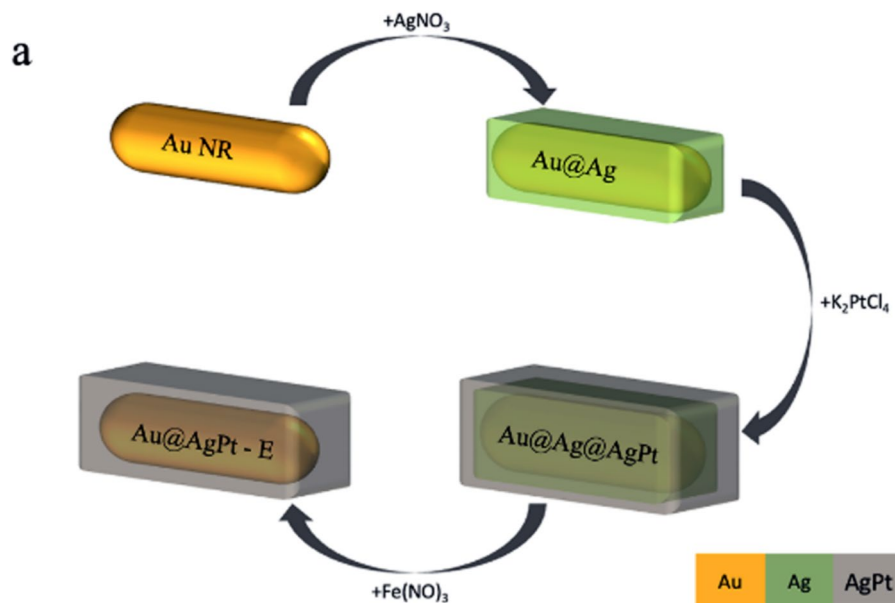
where  $\epsilon_{Pt}$ ,  $\epsilon_{Ag}$ , and  $\epsilon_{eff}$  are the dielectric functions of Pt, Ag, and the composite system (AgPt alloy), respectively.

## Results and discussion

### Materials synthesis and characterization

Figure 1 illustrates the synthesis process of Au@AgPt-E nanoparticles. The process begins with gold-colored Au NRs as the core, followed by the growth of a silver (Ag) shell on the surface by adding an AgNO<sub>3</sub> solution. Then, a gray-black AgPt alloy shell is formed by adding a K<sub>2</sub>PtCl<sub>4</sub> solution. Finally, Fe(NO<sub>3</sub>)<sub>3</sub> and dilute nitric acid solutions are used for etching to remove excess silver, resulting in the Au@AgPt-E composite structure characterized by gray-black alloy nanoparticles. Figure S1(a) and Fig. S2(a) display the EDS images of Au@Ag<sub>360</sub>@Ag<sub>360</sub>Pt<sub>25</sub> and Au@Ag<sub>360</sub>Pt<sub>25</sub>-E, showing the distribution of Au, Ag, and Pt elements, which also confirm the successful synthesis of the materials. Figures S1 and S2(b)-(c) present the elemental weight percentages and atomic percentages of Au@Ag<sub>360</sub>@Ag<sub>360</sub>Pt<sub>25</sub> and Au@Ag<sub>360</sub>Pt<sub>25</sub>-E. The weight percentage of silver decreases from 62.37% to 28.30%, and its atomic percentage drops from 75.11% to 41.84%. This change verifies the successful etching of silver. Although the amount of Ag significantly decreases after etching, a relatively large proportion of Ag atoms remains, indirectly confirming the presence of the alloy structure.

**Fig. 1** A schematic diagram of the stepwise synthesis process of Au@AgPt-E nanoparticles. The process includes intermediates Au@Ag and Au@Ag@AgPt, as well as the final product Au@AgPt-E. The yellow section represents the Au core; the green layer indicates the silver (Ag) coating, and the gray-black outer layer corresponds to the AgPt formed in the final synthesis stage



This is because elemental Ag is corroded, and only Ag that forms an alloy structure can retain good corrosion resistance, making it difficult to completely remove. We used the final concentrations of  $\text{Pt}^{2+}$  and  $\text{Ag}^+$  in the solution to denote different samples. For example,  $\text{Au@Ag}_x\text{@Ag}_y\text{Pt}_z$ , where  $x \mu\text{M}$  represents the final concentration of  $\text{Ag}^+$  in the solution, and  $y \mu\text{M}$  represents the final concentration of  $\text{Pt}^{2+}$ . Similarly,  $\text{Au@Ag}_x\text{Pt}_y\text{-E}$  indicates a sample where  $x \mu\text{M}$  is the final concentration of  $\text{Ag}^+$ ,  $y \mu\text{M}$  is the final concentration of  $\text{Pt}^{2+}$ , and “E” denotes that the material has undergone erosion.

Figure 2a shows the TEM image of the Au NRs. These Au NRs were synthesized by the seed-mediated growth method [44, 45], with a length of  $84.4 \pm 8.7 \text{ nm}$  and a diameter of  $20.4 \pm 2.6 \text{ nm}$ . Their extinction spectral peak is approximately 830 nm, as shown by the black curve in Fig. 2f. For comparison, we synthesized  $\text{Au@Pt}_{25}$  by adding 0.02 mL of  $\text{K}_2\text{PtCl}_4$  solution, with its TEM image shown in Fig. 2b and extinction spectrum in Fig. 2f as the green curve. Compared to Au NRs, the extinction spectrum of  $\text{Au@Pt}_{25}$  exhibits a significant redshift with a decreased extinction peak at approximately 980 nm. This nanostructure measures  $90.0 \pm 8.9 \text{ nm}$  in length and  $26.6 \pm 2.4 \text{ nm}$  in diameter, with dendritic protrusions of Pt observed on the Au NRs surface. Maintaining a constant concentration of AA, the Pt shell layer thickened as the  $\text{K}_2\text{PtCl}_4$  volume increased from

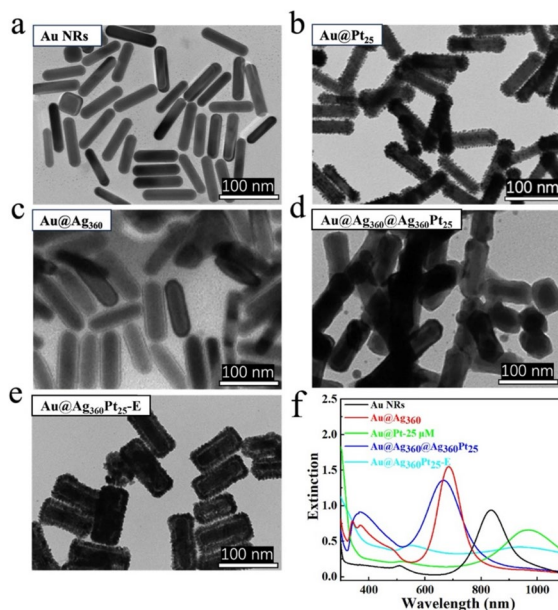


**Fig. 2** a–d TEM images of the products generated during the synthesis of  $\text{Au@Ag}_{360}\text{Pt}_{25}\text{-E}$  and  $\text{Au@Pt}_{25}$  used as a control. a TEM image of Au NRs, b  $\text{Au@Pt}_{25}$ , c  $\text{Au@Ag}_{360}$ , d  $\text{Au@Ag}_{360}\text{@Ag}_{360}\text{Pt}_{25}$ , e  $\text{Au@Ag}_{360}\text{Pt}_{25}\text{-E}$ , with the scale bar in the lower right corner indicating 100 nm, and f their corresponding UV–vis extinction spectra

0.02 to 0.08 mL, resulting in an increased number of surface protrusions, as shown in Fig. S3(a–d). Meanwhile, the extinction spectrum (Fig. S3(e)) further

redshifted with the thickening shell layer. We then synthesized Au@Ag<sub>360</sub> by adding 0.08 mL of AgNO<sub>3</sub> solution to the Au NRs solution. Its TEM image is shown in Fig. 2c, and its extinction spectrum, with a peak at approximately 680 nm, is shown as the red curve in Fig. 2f. This nanostructure has a length of  $95.2 \pm 6.0$  nm and a diameter of  $33.6 \pm 3.6$  nm. Compared to Au NRs, the extinction spectrum exhibits a blueshift with an enhanced peak. With a constant AA concentration, reducing the AgNO<sub>3</sub> volume from 0.08 mL to 0.01 mL resulted in a thinner Ag shell layer, as illustrated in Fig. S4(a-d). The extinction spectrum (Figure S4(e)) indicates a gradual redshift as the shell layer thinned. Next, by adding 0.02 mL of AgNO<sub>3</sub> to the Au@Ag<sub>360</sub> solution, we formed Au@Ag<sub>360</sub>@Ag<sub>360</sub>Pt<sub>25</sub> nanoparticles. Its TEM image is shown in Fig. 2d, and its extinction spectrum, with a peak at approximately 660 nm, is represented by the blue curve in Fig. 2f. This nanostructure measures  $97.2 \pm 8.2$  nm in length and  $38.3 \pm 5.6$  nm in diameter. Compared to Au@Ag<sub>360</sub>, the extinction spectrum shows further blueshift and a reduced peak, primarily due to the formation of independent Ag particles observed in the TEM image, caused by the excess AgNO<sub>3</sub>. Finally, by adding Fe(NO<sub>3</sub>)<sub>3</sub> solution to the Au@Ag<sub>360</sub>@Ag<sub>360</sub>Pt<sub>25</sub> solution to remove the Ag shell layer in Au@Ag<sub>360</sub>@Ag<sub>360</sub>Pt<sub>25</sub> particles, as well as the Ag on the AgPt shell surface, we obtained Au@Ag<sub>360</sub>Pt<sub>25</sub>-E nanoparticles. Its TEM image is shown in Fig. 2e, and its extinction spectrum, with a peak at approximately 930 nm, is represented by the cyan curve in Fig. 2f. This nanostructure has a length of  $96.5 \pm 6.4$  nm and a diameter of  $37.4 \pm 4.8$  nm. Compared to Au@Ag<sub>360</sub>@Ag<sub>360</sub>Pt<sub>25</sub>, the structure's size changed little due to the AgPt shell's stability, which remained unaffected by Fe(NO<sub>3</sub>)<sub>3</sub> corrosion. However, the AgPt shell's surface became rougher as the Ag was removed. The extinction spectrum shows a redshift with a reduced peak.

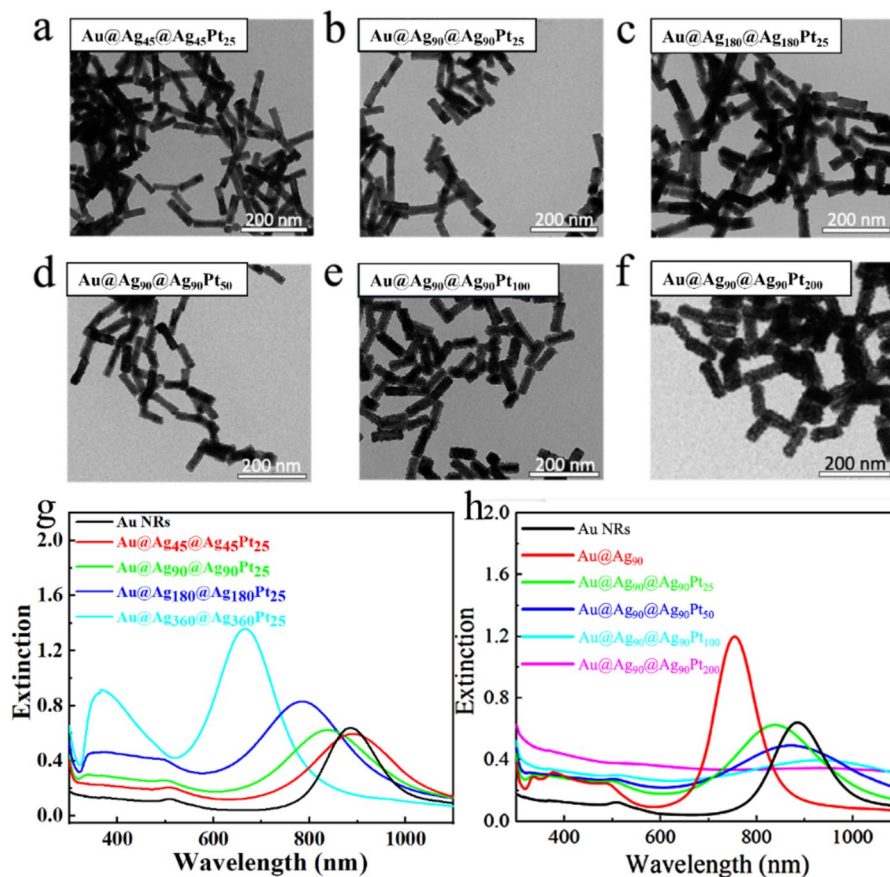
The effect of AgNO<sub>3</sub> and K<sub>2</sub>PtCl<sub>4</sub> dosage on the synthesis of Au@Ag@AgPt

Figure 3a–c displays the TEM images of Au@Ag<sub>45</sub>@Ag<sub>45</sub>Pt<sub>25</sub>, Au@Ag<sub>90</sub>@Ag<sub>90</sub>Pt<sub>25</sub>, and Au@Ag<sub>180</sub>@Ag<sub>180</sub>Pt<sub>25</sub>, respectively. According to Table S1, as the amount of AgNO<sub>3</sub> increases, the length of these nanoparticles increases from  $91.6 \pm 7.3$  to  $94.3 \pm 7.4$  nm, and the diameter increases from  $27.4 \pm 5.2$  to

$33.5 \pm 3.7$  nm. It is evident that under the same conditions, the size of the nanoparticles increases with the amount of AgNO<sub>3</sub>. Meanwhile, as shown in Fig. 3g, their UV–vis extinction spectra exhibit a gradual blue-shift with increasing extinction peak value. Figure 3d–f depicts the TEM images of Au@Ag<sub>90</sub>@Ag<sub>90</sub>Pt<sub>50</sub>, Au@Ag<sub>90</sub>@Ag<sub>90</sub>Pt<sub>100</sub>, and Au@Ag<sub>90</sub>@Ag<sub>90</sub>Pt<sub>200</sub>, respectively. As the amount of K<sub>2</sub>PtCl<sub>4</sub> increases, the length of these nanoparticles increases from  $93.4 \pm 9.2$  to  $103.5 \pm 12.4$  nm, and the diameter increases from  $29.4 \pm 7.3$  to  $40.5 \pm 8.3$  nm. It is clear that under the same conditions, the size of the nanoparticles increase with the amount of K<sub>2</sub>PtCl<sub>4</sub>. Simultaneously, as shown in Fig. 3g, their UV–vis extinction spectra gradually exhibit a red-shift with decreasing extinction peak value.

It can be concluded from the comparison that the amount of K<sub>2</sub>PtCl<sub>4</sub> has a more significant effect on the morphology of the nanomaterials compared to the amount of AgNO<sub>3</sub>. Specifically, as the amount of AgNO<sub>3</sub> increases, the appearance of the nanomaterials does not change much, and the size changes are also relatively small, with the length increasing only from  $91.6 \pm 7.3$  to  $94.3 \pm 7.4$  nm, and the diameter increasing from  $27.4 \pm 5.2$  to  $33.5 \pm 3.7$  nm. In contrast, the increase in the amount of K<sub>2</sub>PtCl<sub>4</sub> leads to more pronounced changes in the size of the nanomaterials, with significant changes in morphology as the surface becomes increasingly rough. This may be due to the fact that, when the AgNO<sub>3</sub> volume is high and the K<sub>2</sub>PtCl<sub>4</sub> volume is low, Pt<sup>2+</sup> primarily acts to etch the Ag shell layer. However, when the AgNO<sub>3</sub> volume is low and the K<sub>2</sub>PtCl<sub>4</sub> volume is high, Pt<sup>2+</sup> not only etches the Ag shell layer but also promotes the growth of the shell. Therefore, compared to AgNO<sub>3</sub>, K<sub>2</sub>PtCl<sub>4</sub> has a more significant impact on the morphology of the nanomaterials. By controlling the amount of AgNO<sub>3</sub> (ranging from 0.02 to 0.16 mL) and varying the amount of K<sub>2</sub>PtCl<sub>4</sub> (from 0.01 to 0.08 mL), we successfully synthesized different materials. Their TEM images are shown in Figs. S5–8(d). These materials were then subjected to etching treatment, and the corresponding TEM images after etching are shown in Figs. S5–8(e–h). The corresponding spectroscopic data are presented in Figs. S5–8(i). When the amounts of AgNO<sub>3</sub> and K<sub>2</sub>PtCl<sub>4</sub> were either too low or too high, the morphological changes before and after etching were minimal. In contrast, when a larger amount of AgNO<sub>3</sub> and a smaller amount of K<sub>2</sub>PtCl<sub>4</sub>

**Fig. 3** **a–c** The TEM images of nanoparticles obtained by adjusting the amount of  $\text{AgNO}_3$  solution (from 0.02 to 0.08 mL) while keeping the  $\text{K}_2\text{PtCl}_4$  volume constant at 0.01 mL: **a** 0.02 mL  $\text{AgNO}_3$ , **b** 0.04 mL  $\text{AgNO}_3$ , and **c** 0.08 mL  $\text{AgNO}_3$ . **d–f** The TEM images of nanoparticles obtained by adjusting the amount of  $\text{K}_2\text{PtCl}_4$  solution (from 0.02 to 0.08 mL) while keeping the  $\text{AgNO}_3$  volume constant at 0.04 mL: **d** 0.02 mL  $\text{K}_2\text{PtCl}_4$ , **e** 0.04 mL  $\text{K}_2\text{PtCl}_4$ , and **f** 0.08 mL  $\text{K}_2\text{PtCl}_4$ . The scale bar is 200 nm, and **g** the UV–vis extinction spectra of nanoparticles with different amounts of  $\text{AgNO}_3$ . **h** The UV–vis extinction spectra with different amounts of  $\text{K}_2\text{PtCl}_4$



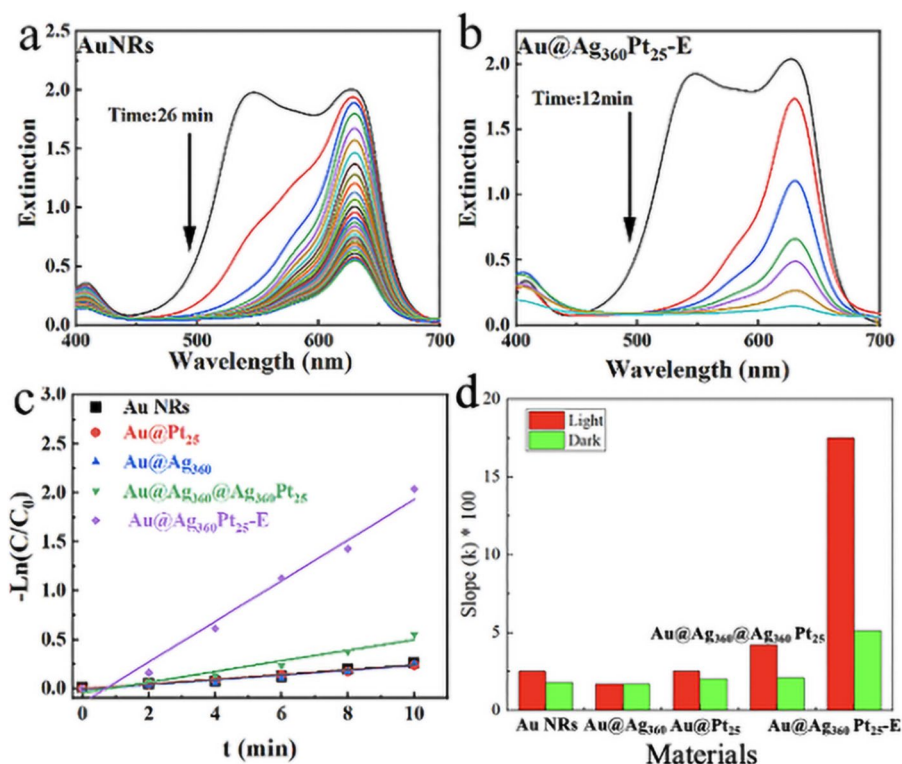
were used, the etched materials exhibited a more pronounced hollow structure. Additionally, the spectroscopic data of the etched materials showed a redshift compared to the non-etched materials, indicating a change in their optical properties.

#### Catalytic reduction of MB and photothermal effects of materials

To evaluate the photocatalytic performance of the materials, we conducted a series of experiments using MB as a model compound. In this study, we chose to use a xenon lamp ( $\lambda > 420$  nm) under light irradiation with  $\text{NaBH}_4$  to reduce MB as the model reaction system; the role of  $\text{NaBH}_4$  in the reaction is solely as a reducing agent. After reduction, MB is converted into the colorless leuco-methylene blue, causing the solution's color to change from blue to colorless. To monitor the progress of the reaction, UV-vis spectra were recorded over time, primarily analyzing the extinction peak of MB at 628 nm.

Figure 4a and b presents the UV–vis extinction spectra of MB catalyzed by Au NRs and Au@Ag<sub>360</sub>Pt<sub>25</sub>-E, respectively, obtained using a spectrometer. Each measurement interval was precisely controlled at 2 min, including 90 s of xenon lamp irradiation and 30 s of spectral collection, resulting in a total of 20 measurements over a 40-min experimental duration. The UV–visible extinction spectra of MB in Fig. 4a and b under different catalytic materials show that, as the photocatalytic process progresses, the extinction peak of MB gradually decreases, and the solution's color fades from blue to colorless. To further analyze the catalytic efficiency, we used the extinction peak at 628 nm as a reference, plotting the reaction kinetics curve based on the equation  $-\ln(C/C_0) = kt$ , as shown in Fig. 4c. The  $k$  values for Au NRs, Au@Pt<sub>25</sub>, Au@Ag<sub>360</sub>, Au@Ag<sub>360</sub>@Ag<sub>360</sub>Pt<sub>25</sub>, and Au@Ag<sub>360</sub>Pt<sub>25</sub>-E are as follows: 0.025, 0.025, 0.017, 0.042, and 0.175. Here,  $C$  represents the extinction peak value of MB at 628 nm at a specific time,  $C_0$  is the initial extinction peak value at 628 nm

**Fig. 4** Photocatalytic performance of different materials. **a** The extinction spectrum of MB during the photocatalytic process of Au NRs; **b** the extinction spectrum of MB during the photocatalytic process of Au@Ag<sub>360</sub>Pt<sub>25</sub>-E; **c** the corresponding rate graph of Au NRs, Au@Pt<sub>25</sub>, Au@Ag<sub>360</sub>, Au@Ag<sub>360</sub>@Ag<sub>360</sub>Pt<sub>25</sub>, and Au@Ag<sub>360</sub>Pt<sub>25</sub>-E; and **d** comparison graph of the  $k * 100$  values for photocatalytic and catalytic reactions of Au NRs, Au@Ag<sub>360</sub>, Au@Pt<sub>25</sub>, Au@Ag<sub>360</sub>@Ag<sub>360</sub>Pt<sub>25</sub>, and Au@Ag<sub>360</sub>Pt<sub>25</sub>-E



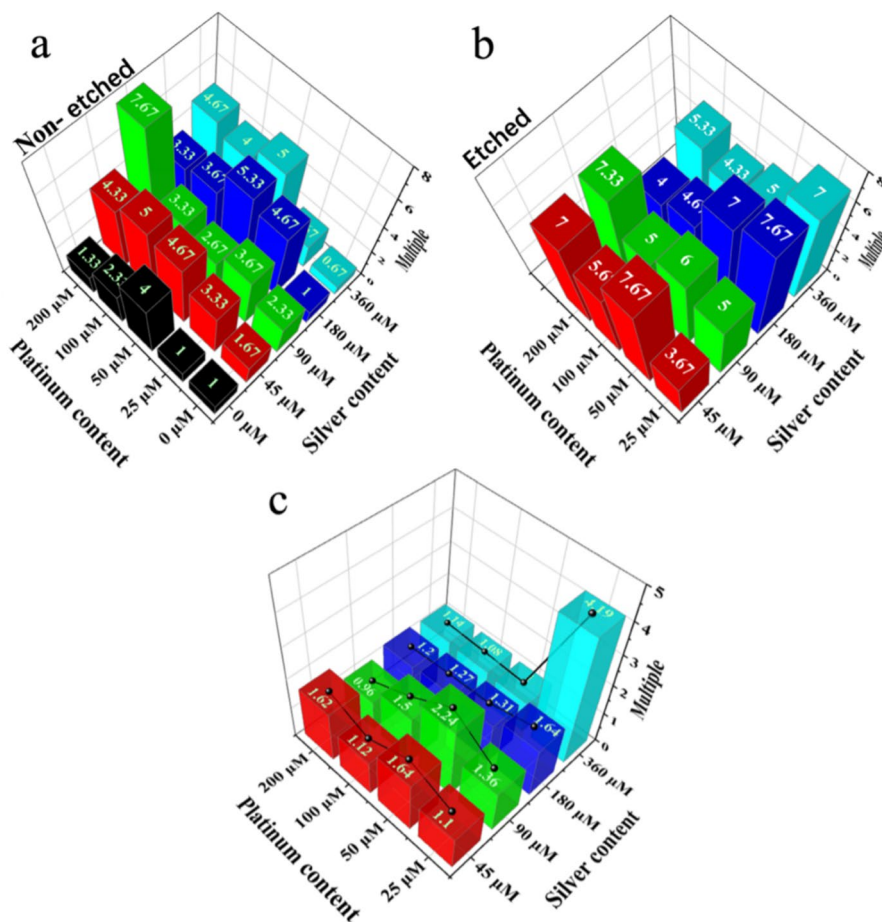
at the start of the reaction, and  $t$  is the elapsed time during the experiment.

Using the equation  $-\ln(C/C_0) = kt$ , we calculated the rate constants for Au NRs, Au@Pt<sub>25</sub>, Au@Ag<sub>360</sub>, Au@Ag<sub>360</sub>@Ag<sub>360</sub>Pt<sub>25</sub>, and Au@Ag<sub>360</sub>Pt<sub>25</sub>-E using MB as the model reaction system. When using Au NRs as the catalyst, complete conversion of MB was not achieved even after the maximum experimental duration. In contrast, when using Au@Ag<sub>360</sub>Pt<sub>25</sub>-E as the catalyst, MB was almost entirely reduced within approximately 12 min, with the photocatalytic rate being 7 times faster than that of Au NRs. To verify the photothermal effect brought by the LSPR effect, we have conducted catalytic comparison experiments in a dark environment without light. The catalytic spectra are shown in Figure S9(a)-(d). Figure 4d presents a comparison graph of the  $k * 100$  values under photocatalytic and catalytic conditions. Under dark conditions, the catalytic efficiency of all materials decreased compared to light conditions. However, Au@Ag<sub>360</sub>Pt<sub>25</sub>-E still exhibited an outstanding catalytic rate under dark conditions, which can mainly be attributed to its larger contact surface area and more catalytic active sites.

To facilitate a more precise comparison, we use the slope of the linear fit as an indicator of catalytic activity, with the slope of Au nanorods serving as the reference standard. Figure 5a and b illustrates the photocatalytic rates before and after etching; specific values are found in tables S2-3, while the catalytic UV-vis extinction spectra of MB are detailed in Figs. S10(a-i) and S11-14(a-h). The various catalytic materials are defined by the final concentrations of the catalyst in their respective synthetic solutions. In Fig. 5a and b, “platinum content” refers to the final concentration of K<sub>2</sub>PtCl<sub>4</sub> in the catalytic material solution, and “silver content” refers to the final concentration of AgNO<sub>3</sub>. For instance, Au@Ag<sub>x</sub>@Ag<sub>x</sub>Pt<sub>y</sub> represents the unetched material with  $x$  μM silver content and  $y$  μM platinum content, while Au@Ag<sub>x</sub>Pt<sub>y</sub>-E refers to the etched material with the same silver and platinum concentrations. The term “Multiple” refers to the fold increase in photocatalytic performance relative to Au NRs.

The results indicate that Au@Ag<sub>90</sub>@Ag<sub>90</sub>Pt<sub>200</sub> and Au@Ag<sub>180</sub>Pt<sub>25</sub>-E exhibit the highest photocatalytic efficiency, reaching approximately 7.67 times that of the Au NRs. And the photocatalytic performance of

**Fig. 5** Comparison of photocatalytic performance before and after material etching. **a** Photocatalytic rate plot of all unetched materials. **b** Corresponding photocatalytic rate plot of the materials after etching. **c** Photocatalytic enhancement rate plot of the materials after etching



Au@Ag<sub>360</sub>Pt<sub>25</sub>-E in the MB reduction reaction shows a significant improvement compared to Au NRs, and it outperforms previously reported Au, Pt, as well as bimetallic or trimetallic-based nanocatalysts. Specific comparison data are found in table S4. In contrast, the photocatalytic rates of Au@Ag<sub>180</sub> and Au@Pt<sub>25</sub> are nearly identical to those of Au nanorods, while the photocatalytic efficiency of Au@Ag<sub>360</sub> is lower than that of Au NRs. This decline in performance could be attributed to an excessive amount of AgNO<sub>3</sub>, which may cause material aggregation, thereby reducing catalytic efficiency.

To further assess the impact of etching on the photocatalytic performance, we compared the catalytic rates before and after the etching process. Figure 5c presents the enhancement in photocatalytic performance for the corresponding catalytic materials after etching, relative to the unetched materials; the specific values are found in table S5. “Multiple”

here refers to the fold increase in photocatalytic efficiency of the material post-etching compared to the unetched version. The linear slope graphs are provided in Figs. S8-11(i-l). As shown in Fig. 5c, the photocatalytic rate of Au@Ag<sub>360</sub>Pt<sub>25</sub>-E significantly improves after etching, exhibiting an approximately 4.19 times increase compared to the unetched Au@Ag<sub>360</sub>Pt<sub>25</sub>.

To explore the reasons for the enhancement of Au@Ag<sub>360</sub>Pt<sub>25</sub>-E, we conducted relevant mechanistic studies. Figure 6(a) and (b) is schematic diagrams of MB molecules and leucomethylene blue molecules, respectively. After the reaction, MB converts into leucomethylene blue, and the actual reaction diagram is shown in Fig. 6(c) and (d). In the experiment, MB was placed in a container, and nanoparticles and a certain amount of NaBH<sub>4</sub> solution were added. When the reaction time reaches 90 s, the container is placed in the spectrometer for UV–vis extinction spectra

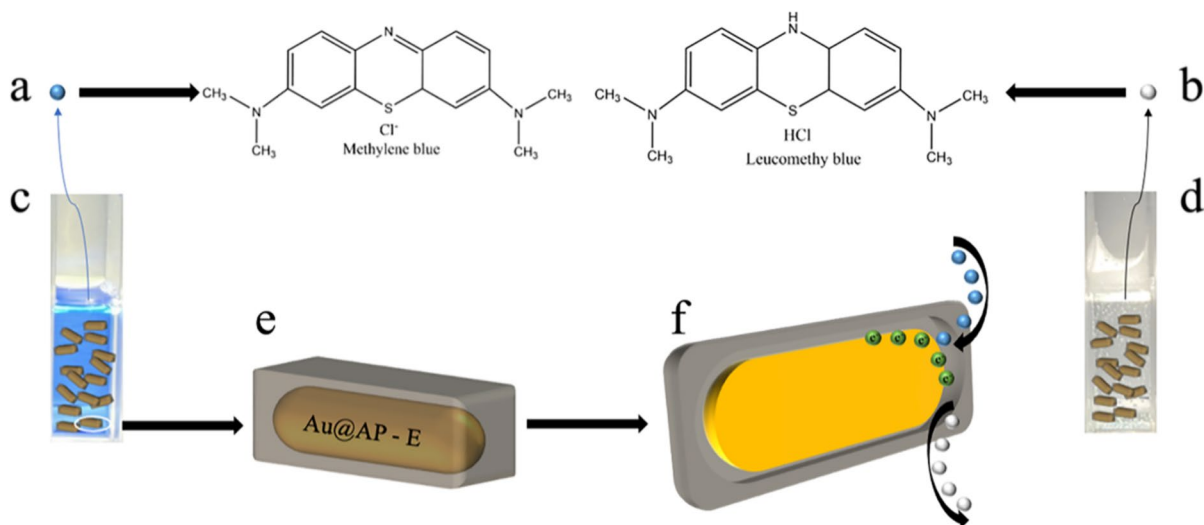


**Fig. 6** **a** The blue spheres represent MB molecules, **(b)** the white spheres represent leucomethylene blue molecules, **(c)** the state inside the container at the beginning of the experiment, **(d)** the state inside the container at the end of the experiment,

**(e)** an enlarged image of Au@AgPt-E inside the container, and **(f)** the reaction mechanism diagram of MB entering Au@AgPt-E

measurement, which takes a total of 30 s. When the reaction was nearly complete, the color inside the container changed from blue to transparent white.

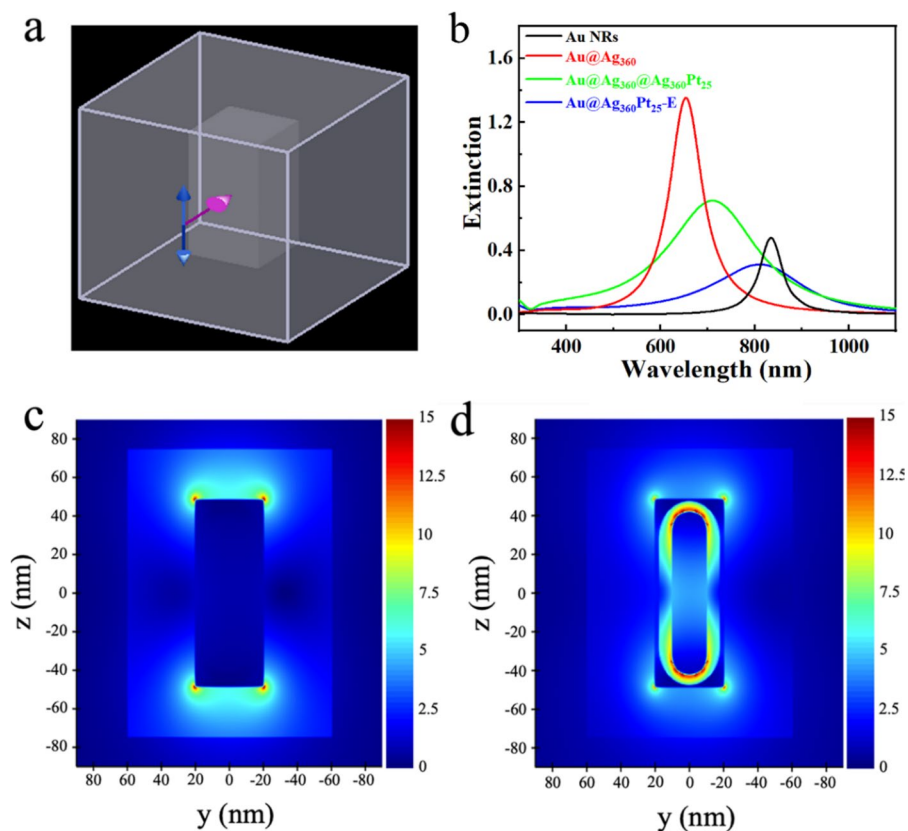
Dey's group [46] assembled a plasmonic nanocomposite system consisting of NiO/Au/[Co(1,10-phenanthroline-5-amine) $_2$ (H $_2$ O) $_2$ ], demonstrating that the LSPR effect can generate hot electrons, which are transferred to cobalt and participate in the hydrogen evolution reaction. During our reaction, due to light irradiation ( $\lambda > 420$  nm), as shown in Fig. 6(e), the Au NRs core in Au@Ag $_{360}$ Pt $_{25}$ -E demonstrates a pronounced LSPR effect. This effect excites a large number of high-energy hot electrons (depicted as green spheres in Fig. 6(f)), which can directly participate in the reaction between MB and NaBH $_4$ . Additionally, due to the LSPR effect, part of the light energy is converted into localized heat, further enhancing the overall thermal efficiency of the reaction system. The AgPt alloy shell also exhibits an LSPR effect [47], generating hot electrons that directly engage in surface reactions. The combined effect of hot electron injection and thermal energy not only promotes the generation and spatial separation of charge carriers but also boosts photocatalytic performance. Moreover, the hollow structure of Au@Ag $_{360}$ Pt $_{25}$ -E, compared to the Au@Ag $_{360}$ @Ag $_{360}$ Pt $_{25}$  structure, provides a larger surface area for contact and more

catalytic active sites, thereby facilitating further enhancement of the photocatalytic rate. As a result, the LSPR effect of Au NRs in Au@Ag $_{360}$ Pt $_{25}$ -E generates more hot electrons and thermal energy, while the AgPt alloy shell and hollow structure offer a larger surface area and additional catalytic active sites, leading to a significant increase in the photocatalytic rate.

#### FDTD simulations

To further validate our mechanism, we conducted FDTD simulations on Au NRs, Au@Ag $_{360}$ , Au@Ag $_{360}$ @Ag $_{360}$ Pt $_{25}$ , and Au@Ag $_{360}$ Pt $_{25}$ -E. Figure 7a shows the model diagram of Au@Ag $_{360}$ Pt $_{25}$ -E, and the models of other nanoparticles are shown in Fig. S15(a-c). Their size data were set according to the actual experimental data, as shown in table S6. Figure 7b shows the simulated extinction UV-vis extinction spectra of Au NR, Au@Ag $_{360}$ , Au@Ag $_{360}$ @Ag $_{360}$ Pt $_{25}$ , and Au@Ag $_{360}$ Pt $_{25}$ -E. The black curve represents the extinction spectrum of Au NR; the red curve represents the extinction spectrum of Au@Ag $_{360}$ ; the green curve represents the extinction spectrum of Au@Ag $_{360}$ @Ag $_{360}$ Pt $_{25}$ , and the blue curve represents the extinction spectrum of Au@Ag $_{360}$ Pt $_{25}$ -E. The trend of these UV-vis extinction spectra is consistent with the extinction UV-vis

**Fig. 7** **a** The model diagrams of the Au@Ag<sub>360</sub>Pt<sub>25</sub>-E; **b** the FDTD simulated extinction spectra of Au NRs, Au@Ag, Au@Ag<sub>360</sub>@Ag<sub>360</sub>Pt<sub>25</sub>, and Au@Ag<sub>360</sub>Pt<sub>25</sub>-E; and the FDTD simulated electric field distribution diagrams of **c** Au@Ag<sub>360</sub>@Ag<sub>360</sub>Pt<sub>25</sub> and **d** Au@Ag<sub>360</sub>Pt<sub>25</sub>-E



extinction spectra measured in the experiment, except for Au@Ag<sub>360</sub>@Ag<sub>360</sub>Pt<sub>25</sub>. We believe that this difference may be due to the relatively fast reaction rate during the formation of Au@Ag<sub>360</sub>@Ag<sub>360</sub>Pt<sub>25</sub> and the large amount of AgNO<sub>3</sub> solution added, which led to the generation of some silver nanoparticles in the experiment, as shown in Fig. 2d. Additionally, there are differences in particle uniformity, and the morphology is not as smooth as the simulated model. These factors collectively contributed to the discrepancy between the experimental extinction spectra (Fig. 2f) and the FDTD simulation results (Fig. 7b). However, the trends in the changes of the spectral data from the FDTD simulation are generally consistent with those observed in the experimental spectra.

Figure 7c and d respectively shows the FDTD simulated electric field diagrams of Au@Ag<sub>360</sub>@Ag<sub>360</sub>Pt<sub>25</sub> and Au@Ag<sub>360</sub>Pt<sub>25</sub>-E, with the electric field diagrams of other materials shown in Fig. S15(d-e). From the electric field diagram of Au@Ag<sub>360</sub>Pt<sub>25</sub>-E, it can be seen that compared to Au@Ag<sub>360</sub>@Ag<sub>360</sub>Pt<sub>25</sub>, the electric field intensity is higher, primarily due to

the combined effect of Au NRs and the AgPt shell. It is observed in the diagram that the electric field inside the Au NRs and at the AgPt shell is stronger, further confirming that Au@Ag<sub>360</sub>Pt<sub>25</sub>-E exhibits an LSPR effect, which in turn promotes the generation of hot electrons in the Au NRs core and the AgPt shell. Ultimately, the synergistic effect of these hot electrons inside Au@Ag<sub>360</sub>Pt<sub>25</sub>-E and on the AgPt alloy surface together enhances the photocatalytic performance.

## Conclusions

In this study, the Au@AgPt-E nanostructure was prepared through a multi-step chemical reaction. This material exhibited excellent photocatalytic performance, showing significant activity enhancement in the reduction of MB, which was attributed to the design of the hollow multilayer alloy structure. FDTD simulations verified the experimental results, showing that this nanostructure has a strong local electromagnetic field enhancement effect under light irradiation,

significantly increasing the generation efficiency of photogenerated electron–hole pairs and accelerating the catalytic reaction rate. By comparing their catalytic and photocatalytic performances, it was further confirmed that the photothermal effect induced by the LSPR effect contributes to the improvement of photocatalytic efficiency.

The study also explored the principles and mechanisms behind the material design, emphasizing the surface plasmon resonance effect of the Au NRs core, the optimization of photogenerated carrier separation efficiency by the hollow structure, and the high activity catalytic provided by the outer Pt element.

**Acknowledgements** The authors thank Sudan Shen for her assistance in TEM at State Key Laboratory of Chemical Engineering (Zhejiang University). T. S. Deng acknowledge financial support from Zhejiang Provincial Natural Science Foundation (Grant: LY24F050008), and National Natural Science Foundation of China (NSFC, Grant: 61905056).

**Author Contribution** T.S.D. initiated the project. C.Y.C. and Y.Q.D. were supervised by T.S.D. C.Y.C. completed relevant experiments, FDTD simulations, and wrote dissertations. Y.Q.D. contributed to data analysis and discussion. All the authors gave comments on the manuscript.

**Data Availability** No datasets were generated or analysed during the current study.

#### Declarations

**Competing interests** The authors declare no competing interests.

## References

- Lu WS, Wang HF, Zhang JP et al (2015) Gold nanorods: synthesis, growth mechanism and purification. *Prog Chem* 27:785–793. <https://doi.org/10.7536/pc150111>
- Al-Zubeidi A, Hoener BS, Collins SSE et al (2019) Hot holes assist plasmonic nanoelectrode dissolution. *Nano Lett* 19:1301–1306. <https://doi.org/10.1021/acs.nanolett.8b04894>
- Ben-Shahar Y, Scotognella F, Kriegel I et al (2016) Optimal metal domain size for photocatalysis with hybrid semiconductor-metal nanorods. *Nat Commun* 7:10413. <https://doi.org/10.1038/ncomms10413>
- Mbalaha ZSS, Birch DJS, Chen Y (2023) Photothermal effects of gold nanorods in aqueous solution and gel media: Influence of particle size and excitation wavelength. *IET Nanobiotechnol* 17:103–111. <https://doi.org/10.1049/nbt2.12110>
- Okuno T, Kawamura G, Muto H et al (2014) Fabrication of shape-controlled Au nanoparticles in a TiO<sub>2</sub>-containing mesoporous template using UV irradiation and their shape-dependent photocatalysis. *J Mater Sci Technol* 30:8–12. <https://doi.org/10.1016/j.jmst.2013.08.008>
- Di ZY, Schultz I, Yi ZH et al (2014) Surface-enhanced Raman scattering on template-embedded gold nanorod substrates. *J Mod Opt* 61:72–76. <https://doi.org/10.1080/09500340.2013.854420>
- Suzuki M, Nidome Y, Terasaki N et al (2004) Surface-enhanced nonresonance Raman scattering of rhodamine 6G molecules adsorbed on gold nanorod films. *Jpn J Appl Phys* 43:L554–L556. <https://doi.org/10.1143/jjap.43.L554>
- Tao J, Lu YH, Chen JX et al (2011) Polarization-dependent surface-enhanced Raman scattering via aligned gold nanorods in poly(vinyl alcohol) film. *Plasmonics* 6:785–789. <https://doi.org/10.1007/s11468-011-9265-9>
- Xie ZG, Tao J, Lu YH et al (2009) Polymer optical fiber SERS sensor with gold nanorods. *Opt Commun* 282:439–442. <https://doi.org/10.1016/j.optcom.2008.10.018>
- Ming T, Zhao L, Yang Z et al (2009) Strong polarization dependence of plasmon-enhanced fluorescence on single gold nanorods. *Nano Lett* 9:3896–3903. <https://doi.org/10.1021/nl902095q>
- Peng L, Liu Y, Zhang J et al (2022) Surface plasmon-enhanced NIR-II fluorescence in a multilayer nanoprobe for through-skull mouse brain imaging. *ACS Appl Mater Interfaces* 14:38575–38583. <https://doi.org/10.1021/acsami.2c11218>
- Xu SH, Jiang LP, Nie YY et al (2018) Gold nanobipyramids as dual-functional substrates for in situ “turn on” analyzing intracellular telomerase activity based on target-triggered plasmon-enhanced fluorescence. *ACS Appl Mater Interfaces* 10:26851–26858. <https://doi.org/10.1021/acsami.8b05447>
- Yuan H, Lu YX, Wang Z et al (2016) Single nanoporous gold nanowire as a tunable one-dimensional platform for plasmon-enhanced fluorescence. *Chem Commun* 52:1808–1811. <https://doi.org/10.1039/c5cc08149a>
- Alkilany AM, Thompson LB, Boulos SP et al (2012) Gold nanorods: their potential for photothermal therapeutics and drug delivery, tempered by the complexity of their biological interactions. *Adv Drug Delivery Rev* 64:190–199. <https://doi.org/10.1016/j.addr.2011.03.005>
- Chen Y-S, Frey W, Kim S et al (2010) Enhanced thermal stability of silica-coated gold nanorods for photoacoustic imaging and image-guided therapy. *Opt Express* 18:8867–8877. <https://doi.org/10.1364/oe.18.008867>
- Huang XH, El-Sayed IH, El-Sayed MA (2010) Applications of gold nanorods for cancer imaging and photothermal therapy. *Methods Mol Biol* 624:343–357. [https://doi.org/10.1007/978-1-60761-609-2\\_23](https://doi.org/10.1007/978-1-60761-609-2_23)
- Zhang M, Zhang XY, Zhao K et al (2022) Assembly of gold nanorods with L-cysteine reduced graphene oxide for highly efficient NIR-triggered photothermal therapy. *Spectrochim Acta A Mol Biomol Spectrosc* 266:120458. <https://doi.org/10.1016/j.saa.2021.120458>
- Liu M, Yang P-H, Cai J-Y (2009) Optical properties and biomedical application of gold nanorods. *Prog Biochem Biophys* 36:1402–1407. <https://doi.org/10.3724/sp.J.1206.2009.00194>

19. Meireles IBDCJ, Cipreste MF, Gastelois PL et al (2021) Synthesis and characterization of gold nanorods coated by mesoporous silica MCM-41 as a platform bioapplication in photohyperthermia. *Nanotechnol* 32:505720. <https://doi.org/10.1088/1361-6528/ac28db>
20. Pissuwan D, Niidome T (2015) Polyelectrolyte-coated gold nanorods and their biomedical applications. *Nanoscale* 7:59–65. <https://doi.org/10.1039/c4nr04350b>
21. Deng Z-D, Zhang C-C, Li W-T et al (2024) Preparation of Pt@Au hollow nanobipyramid heterostructures for effective photocatalytic degradation. *J Phys Chem C* 128:13007–13014. <https://doi.org/10.1021/acs.jpcc.4c03086>
22. Prasad SN, Mahasivam S, Ramanathan R et al (2024) Silver-based bimetallic nanozyme fabrics with peroxidase-mimic activity for urinary glucose detection. *Anal Bioanal Chem* 416:6149–6159. <https://doi.org/10.1007/s00216-024-05483-7>
23. Wang C, Wang L, Nallathambi V et al (2024) Structural regulation of Au-Pt bimetallic aerogels for catalyzing the glucose cascade reaction. *Adv Mater* 36:2405200. <https://doi.org/10.1002/adma.202405200>
24. Xuan C, Cao Y, Wu H et al (2024) Bioinspired core-shell nanospheres integrated in multi-signal immunochromatographic sensor for high throughput sensitive detection of Bongkrekic acid in food. *Food Chem* 460:140565. <https://doi.org/10.1016/j.foodchem.2024.140565>
25. Fathima R, Mujeeb A (2021) Enhanced nonlinear and thermo optical properties of laser synthesized surfactant-free Au-Pt bimetallic nanoparticles. *J Mol Liq* 343:117711. <https://doi.org/10.1016/j.molliq.2021.117711>
26. Shiraiishi T, Takuma Y, Miura E et al (2003) Factors affecting the optical properties of Pd-free Au-Pt-based dental alloys. *J Mater Sci Mater Med* 14:1021–1026. <https://doi.org/10.1023/B:JMSM.0000003997.45001.2e>
27. Yang Y, Chen M, Wu YJ et al (2019) Ultrasound assisted one-step synthesis of Au@Pt dendritic nanoparticles with enhanced NIR absorption for photothermal cancer therapy. *RSC Adv* 9:28541–28547. <https://doi.org/10.1039/c9ra04286e>
28. Kim YH, Kim AY, Kim GH et al (2016) Electrochemical and in vitro neuronal recording characteristics of multi-electrode arrays surface-modified with electro-co-deposited gold-platinum nanoparticles. *Biomed Microdevices* 18:1–7. <https://doi.org/10.1007/s10544-016-0044-4>
29. Liu W, Zhao NN, Yin Q et al (2023) Injectable hydrogels encapsulating dual-functional Au@Pt core-shell nanoparticles regulate infarcted microenvironments and enhance the therapeutic efficacy of stem cells through antioxidant and electrical integration. *ACS Nano* 17:2053–2066. <https://doi.org/10.1021/acsnano.2c07436>
30. Muniramaiah R, Fernandes JM, Raja MM et al (2022) Mechanically stable ultrathin flexible metallic Au/Pt/Au tri-layer as an alternative transparent conducting electrode for optoelectronic device applications. *Vacuum* 206:111487. <https://doi.org/10.1016/j.vacuum.2022.111487>
31. Zhou J, Xia G, Li B et al (2003) Structural and electrical properties of Au/Pt/Ti ohmic contacts to degenerated doped n-GaAs. *Appl Phys A* 76:939–942. <https://doi.org/10.1007/s00339-002-1439-z>
32. Dimitratos N, Villa A, Wang D et al (2006) Pd and Pt catalysts modified by alloying with Au in the selective oxidation of alcohols. *J Catal* 244:113–121. <https://doi.org/10.1016/j.jcat.2006.08.019>
33. Kaizuka K, Lee K-Y, Miyamura H et al (2012) Multiphase flow systems for selective aerobic oxidation of alcohols catalyzed by bimetallic nanoclusters. *J Flow Chem* 2:1–4. <https://doi.org/10.1556/jfchem.2011.00014>
34. Grad O, Dan M, Mihet M et al (2024) MIL-101(Cr) supported Pt and Au-Pt composites as active catalysts for the selective hydrogenation of nitrobenzene under mild reaction conditions. *Surf Interfaces* 51:104729. <https://doi.org/10.1016/j.surf.2024.104729>
35. Potrzebowska N, Cardenas L, Derrien E et al (2024) Ultrasonication-assisted preparation of Au-Pt/ZrO<sub>2</sub> catalysts for the selective base-free oxidation of glucose to glucaric acid. *ChemCatChem* 16:e202400338. <https://doi.org/10.1002/cctc.202400338>
36. Chen L, Kuai L, Yu X et al (2013) Advanced catalytic performance of Au-Pt double-walled nanotubes and their fabrication through galvanic replacement reaction. *Chem-eur J* 19:11753–11758. <https://doi.org/10.1002/chem.201301490>
37. Tan LY, Li LD, Peng Y et al (2015) Synthesis of Au@Pt bimetallic nanoparticles with concave Au nanocuboids as seeds and their enhanced electrocatalytic properties in the ethanol oxidation reaction. *Nanotechnol* 26:505401. <https://doi.org/10.1088/0957-4484/26/50/505401>
38. Gu Q, Zhu J, Weng G-J et al (2024) Au@AgPt core/cage nanoframes as photothermal catalyst for enhanced NIR-induced 4-nitrophenol reduction. *J Environ Chem Eng* 12:113273. <https://doi.org/10.1016/j.jece.2024.113273>
39. Jung H, Kwon Y, Kim Y et al (2023) Directing energy flow in core-shell nanostructures for efficient plasmon-enhanced electrocatalysis. *Nano Lett* 23:1774–1780. <https://doi.org/10.1021/acs.nanolett.2c04544>
40. Zhou X, Huang HQ, Yang YQ et al (2023) Dendritic alloy shell Au@AgPt yolk sensor with excellent dual SERS enhancement and catalytic performance for in-situ SERS monitoring reaction. *Sensors Actuators B-Chemical* 394:134385. <https://doi.org/10.1016/j.snb.2023.134385>
41. Wu HT, Yang XZ (2024) Biofunctional photoelectrochemical/electrochemical immunosensor based on BiVO<sub>4</sub>/BiOI-MWCNTs and Au@PdPt for alpha-fetoprotein detection. *Bioelectrochemistry* 160:108773. <https://doi.org/10.1016/j.bioelechem.2024.108773>
42. Babar S, Weaver JH (2015) Optical constants of Cu, Ag, and Au revisited. *Appl Opt* 54:477–481. <https://doi.org/10.1364/ao.54.000477>
43. Garnet JCM (1904) X II Colours in metal glasses and in metallic films. *Philos. Trans. R. Soc., A* 203:385–420. <https://doi.org/10.1098/rsta.1904.0024>
44. Abdelmotti LG, Zamborini FP (2010) Potential-controlled electrochemical seed-mediated growth of gold nanorods directly on electrode surfaces. *Langmuir* 26:13511–13521. <https://doi.org/10.1021/la101639u>
45. Qiu Y, Liu Y, Wang LM et al (2010) Surface chemistry and aspect ratio mediated cellular uptake of Au nanorods. *Biomater* 31:7606–7619. <https://doi.org/10.1016/j.biomaterials.2010.06.051>

46. Dey A, Mendalz A, Wach A et al (2024) Hydrogen evolution with hot electrons on a plasmonic-molecular catalyst hybrid system. *Nat Commun* 15:445. <https://doi.org/10.1038/s41467-024-44752-y>
47. Kunwar S, Pandey P, Lee J (2019) Enhanced localized surface plasmon resonance of fully alloyed AgAuPdPt, AgAuPt, AuPt, AgPt, and Pt nanocrystals: systematical investigation on the morphological and LSPR properties of mono-, bi-, tri-, and quad-metallic nanoparticles. *ACS Omega* 4:17340–17351. <https://doi.org/10.1021/acsomega.9b02066>

**Publisher's Note** Springer Nature remains neutral with regard to jurisdictional claims in published maps and institutional affiliations.

Springer Nature or its licensor (e.g. a society or other partner) holds exclusive rights to this article under a publishing agreement with the author(s) or other rightsholder(s); author self-archiving of the accepted manuscript version of this article is solely governed by the terms of such publishing agreement and applicable law.